# Fiber Optic Sensored Geotechnical Testing and Field Monitoring

An-Bin Huang[1], Ph.D., P.E., Yen-Teh Ho[2], Jui-Ting Lee[3], and Chien-Chih Wang[4]

Department of Civil Engineering, National Chiao Tung University,
1001 Ta Hsueh Rd., Hsin Chu, TAIWAN 30050
1. <huanganbin283@gmail.com>
2. <ytho2004@gmail.com>,
3. <juitinglee@gmail.com>
4. <cc.wang.nctu@gmail.com>

**ABSTRACT**   Over the past few decades, many optical fiber sensing techniques have been developed.   Among these available sensing methods, optical fiber Bragg grating (FBG) is probably the most popular.   With its unique capabilities, FBG based geotechnical sensors can be used as a sensor array for distributive (profile) measurements, deployed under water (submersible), for localized high resolution and/or differential measurements.   The authors have developed a series of FBG based transducers that include load cells, linear displacement transducers and gauge/differential pore-pressure sensors.   These transducers have been integrated into a fully FBG sensored triaxial device.   Field in situ testing devices that include pre-bored pressuremeter (PMT), flat dilatometer (DMT) and a piezo-penetrometer have been incorporated with FBG sensors.   Techniques that involve the field installation of FBG inclinometer and pore-pressure sensor arrays for automated slope stability monitoring have been developed.   This paper provides a brief background of FBG and the design concepts behind the FBG based laboratory, in situ testing and field monitoring sensors.   Case histories that include: PMT and triaxial tests on unsaturated soils, field differential pressure piezometer and DMT to characterize a reservoir sediment under 40m of water, and fully automated slope stability monitoring with FBG in place inclinometer and pore pressure arrays are presented.   Implications in geotechnical testing and monitoring are discussed.

## 1.  INTRODUCTION

Electrical sensors have been used in geotechnical testing and field monitoring for more than half a century.   This is especially attractive when the monitoring or testing devices need to be incorporated into an automated system.   Although not always the case, most electrical sensors are non-distributive.   A separate set of cables are required for electrical power supply and/or signal transmission for a given sensor.   Most electrical sensor and cable systems are prone to adverse effects of

electro-magnetic inference (EMI), short circuit, and lightning. Lightning can be especially damaging when the electrical sensors are installed in the field. Because of these drawbacks, electrical sensor systems when deployed in the field in large scale can be bulky, costly, and lack durability. Almost concurrent with the development in optical fiber communication, engineers and scientists have been exploring the potential of using optical fiber as sensors for various purposes. Fiber optic sensors have features that are especially appealing for geotechnical testing or field monitoring where the sensors are often subject to extreme or harsh conditions. Common drawbacks of the electrical sensors can be significantly and readily avoided when using the fiber optic sensors. Of the many available techniques, the authors have been concentrating on the use of Fiber Bragg Grating (FBG) as a core sensing element in their developments of a series of fiber optic sensored geotechnical testing and field monitoring systems. This paper provides a brief background of FBG and presents the experiences in the application of various FBG sensored testing and monitoring systems developed by the authors.

## 2. FBG AS A PARTIALLY DISTRIBUTIVE STRAIN SENSOR

Optical fibers are made of silica, with a diameter about the same of a human hair, and can transmit light over long distances with very little loss of fidelity. Optical fibers comprise two essential components: a core surrounded by an annular cladding. The core of the optical fiber serves to guide light along the length of the optical fiber. The cladding has a slightly lower index of refraction than the core. Its primary function is to ensure total internal reflection within the core and that very little light is lost as it propagates along the core of the optical fiber. The typical combined diameter of core and cladding is 125 μm. The silica core/cladding is protected by an acrylic coating. The total outside diameter of an optical fiber with the acrylic coating is 250 μm. There are other types of optical fibers of different dimensions and materials for various purposes. Readers are referred to Agrawal (2002) for more details on fiber-optic communication systems.

By adopting technologies from telecommunication, many fiber optic based sensing techniques have been developed. These sensors have been used in medical, defense, aeronautical, and civil engineering industries. Development and application of fiber optic sensors are expanding rapidly as indicated by the well-attended conferences organized by many international societies such as the International Society for Optical Engineering (SPIE). The fiber optic Bragg grating (FBG) is one of the many available forms of optical fiber sensors. An FBG is made by a periodic variation of fiber core refractive index. This periodic variation is formed by exposing a 1 to 20 mm long segment of single mode optical fiber to a spatial pattern of ultraviolet light (Hill et al., 1978; Meltz et al., 1989). When the FBG is illuminated by a wideband light source, a fraction of the light is reflected back upon interference by the FBG. The wavelength of the reflected light, or the Bragg wavelength, $\lambda_B$ is related to the period of the index modulation, $\Lambda$, and effective fiber core index of refractive, $n$, as expressed by (Rao, 1998):

$$\lambda_B = 2n\Lambda \tag{1}$$

Longitudinal strains within the Bragg grating, $\varepsilon_B$, induced by variations in temperature or stress can cause a change in $\Lambda$ and thus a shifting of $\lambda_B$, with the following approximate relationships (Rao, 1998):

$$\Delta\lambda_B = 0.74\lambda_B\varepsilon_B \tag{2}$$

and

$$\Delta\lambda_B = 8.9\times10^{-6}\lambda_B\Delta T \tag{3}$$

where $\Delta T$ is the change of temperature in degree Celsius. The constants in Equations (2) and (3) can vary, depending on the photoelastic properties of the optical fiber. For the FBG sensors reported herein, the $\lambda_B$ ranged from 1520 to 1570 nm ($10^{-9}$ m). A typical commercially available FBG data acquisition system can detect a shifting of $\lambda_B$ as small as 1pm ($10^{-12}$ m), which corresponds to a strain ($\varepsilon_B$) of the order of $10^{-6}$ according to Equation (2). This is well above desirable resolution for strain sensors. In addition, the strain $\varepsilon_B$ is determined through the change of $\lambda_B$ which is relatively immune to variations in the strength of light source. This unique feature makes FBG less likely to have signal drifting with time.

The returned signal from every FBG carries a unique domain of wavelength $\lambda_B + \Delta\lambda_B$, making it possible to have multiple FBG elements on the same fiber. The multiplexing among various sensors on a single fiber can be accomplished by wavelength division addressing as conceptually described in Figure 1. Most of the silica optical fiber breaks at a strain of 0.01% which corresponds to a $\Delta\lambda_B$ of approximately 10 nm. Thus, a separation of $\lambda_B$ in 8 to 10 nm between FBG's would be sufficient in most cases. The FBG is partially distributive because only those parts of the optical fiber with FBG are used as strain sensors and these sensors can share the same optical fiber transmission line.

With proper configuration, all advantages of the FBG stated above can be inherited in FBG-based transducers or testing devices for geotechnical engineering monitoring/testing purposes. These advantages can include: capability of being partially distributive, high resolution, good signal stability and immunity to EMI. The FBG can be used directly as a strain gage, or, with the help of mechanical components, FBG can be configured as displacement, pressure and inclination transducers. The FBG based sensors can be used as an individual sensor to reflect the physical quantity at a given location or connected into an array so that the profile of a given or multiple types of physical quantities can be monitored. Typical physical quantities that can be of interest to geotechnical engineering include force, pressure, strain and displacement.
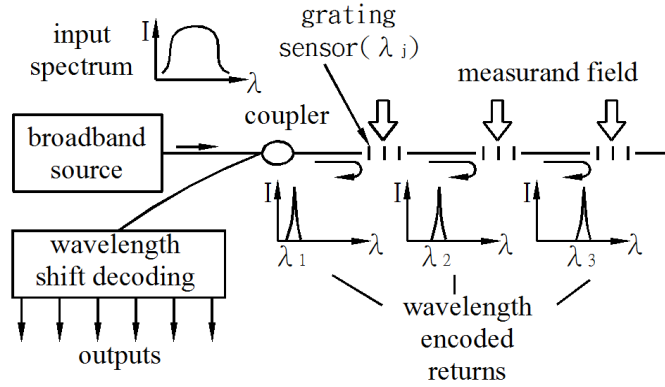
**Fig. 1 Schematic diagram of Fiber Bragg Grating (adapted from Kersey, 1992), I = light intensity λ = wavelength.**

## 3. SLOPE DISPLACEMENT MONITORING AT HUA-FAN UNIVERSITY

An FBG sensored in-place inclinometer (FBG In-Place Inclinometer, FBG-IPI）was developed for the purpose of monitoring variations of inclination in reference to gravity. The pendulum type of design is conceptually depicted in Figure 2. A mass (M) is linked to a hinge. The vertical distance between the hinge and center of gravity of the mass is $L_M$. A pair of FBG's spaced at $d_{FBG}$ from the center line of the pendulum and stemmed from the top end are fixed to the sides of the mass. The FBG pair was used to sense the amount of rotation of the mass and offset the temperature effects. When the mass is rotated away from verticality by an angle (θ) against the hinge, the change in force experienced by the FBG（$\Delta F_{FBG}$）is:

$$\Delta F_{FBG} = \frac{MgL_M \sin\theta}{d_{FBG}} \qquad (4)$$

where g is the gravity. The two FBG's experience the same magnitude of $\Delta F_{FBG}$ but with opposite signs. By subtracting $\Delta F_{FBG}$ of one FBG from the other, the rotation induced FBG wavelength changes are enhanced while the temperature effects are nullified. The key elements of FBG-IPI shown in Figure 2 had a total length of 150 mm, and were sealed in a 30 mm diameter aluminum tube. Spring loaded wheels are fitted to the top and bottom of each FBG-IPI as shown in Figure 3a. These wheels are compatible with the conventional inclinometer casing. A string of FBG-IPI's can be connected into an array and placed in an inclinometer casing for long term, automated ground displacement profile monitoring. Computation of the ground lateral displacement based on the change of inclination from the individual FBG-IPI is the same as that for the interpretation of manual inclinometer probe (IP) readings.
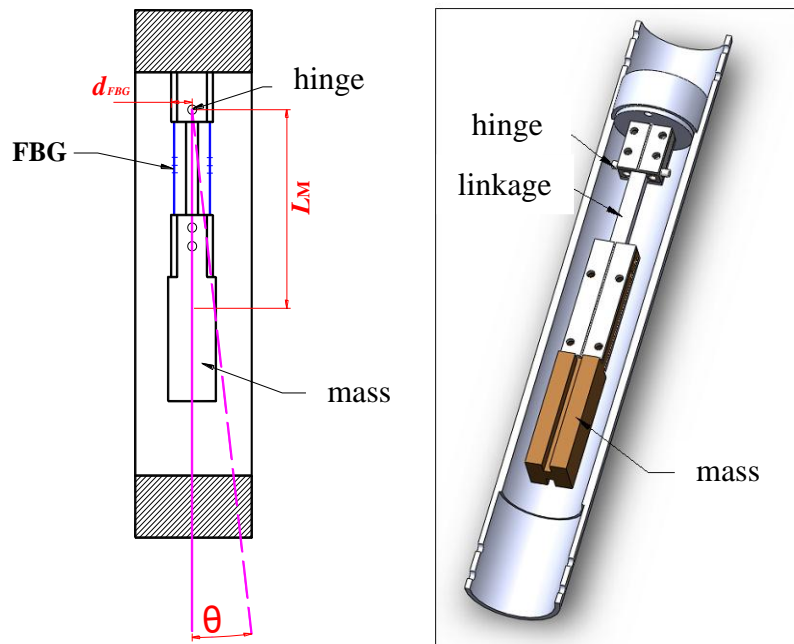
**Fig. 2 Design of the FBG-IPI.**

Figure 3 shows the FBG-IPI's, and their assembly and insertion into an inclinometer casing.  The FBG-IPI's were used to monitor ground movement of a slope in the up-down slope plane, at Hua-Fan University in Shihding Dist., New Taipei City. The university campus was built almost entirely on slopes.  The monitored area was underlain by colluvial material, with occasional steep slope in excess of $25^o$. Each FBG-IPI unit had a length of 1.25 m, capable of measuring inclination with a full range of $\pm 10^o$ and a resolution of $0.0016^o$, in a single plane.   The accuracy of FBG-IPI is $\pm 0.116\%$ full scale.    The FBG-IPI installation consisted of an array of twenty, 1.25 m units extending to 25 m below ground surface.   Installation was completed in August, 2010 and typhoon Megi characterized by heavy rainfall, passed this region in October 2010.   Figure 4 shows a comparison of ground displacement profile according to the FBG-IPI and those from manual IP readings. The manual IP readings were taken from an inclinometer casing located at approximately 40 m off the cross sectional plane where the FBG-IPI's were situated, but with similar ground surface elevation.   Both measurements showed a shear plane at 20 m deep and similar pattern of ground movements, although the magnitudes were different.   The difference in ground displacement magnitude may well be associated with spatial material property variations.

(a) 1.25m long FBG-IPI units      (b) Assembly and insertion of FBG-IPI

**Fig. 3 Installation of FBG-IPI at a Hua-Fan University slope.**

The current FBG-IPI design allows the individual units to be installed at a minimum space of 500 mm.   The FBG-IPI can be rotated $90^{o}$ alternatively during assembly so that displacement in two mutually perpendicular planes can be monitored as in the case of A-A and B-B plane measurements when using the manual IP.
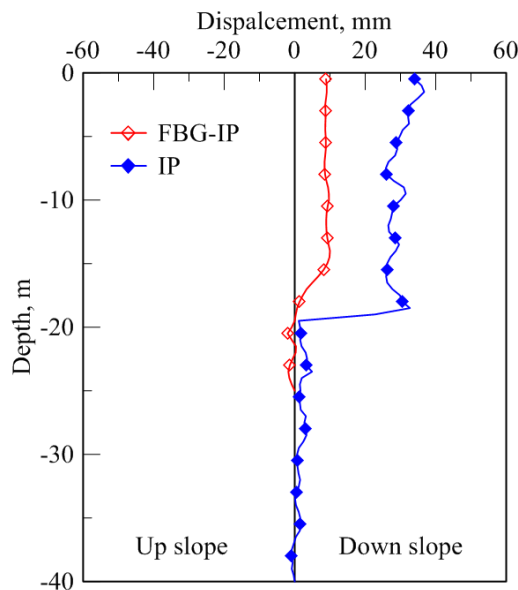


**Fig. 4 Comparison with the neighboring IP readings.**

## 4.  PORE WATER PRESSURE PROFILE MONITORING AT FIVE TURN POINT

A section of Highway 18 that connects Chiayi County to Alishan Mountain, referred to as the Five Turn Point, has been considered as the most dangerous highway in Taiwan.   The Five Turn Point is located in a sloping area of approximately 1200 m by 1000 m, with a topographical relief of up to 400 m.   Figure 5 shows a

topographic map of the general area of Five Turn Point.  At least eight sectors (designated as N1 to N8 in Figure 5) within the Five Turn Point area have been identified with either previous slope failures or signs of continuous movement. The shear planes could reach as much as 80 m below ground surface.  Figure 6 depicts a cross sectional view of section B-B that has an average slope angle of 23$^{\circ}$. The shear planes associated with earlier ground failures according to available investigations are also included in Figure 6.  The subject area was covered by 0-26 m of colluvial material that consisted of a mixture of soil and rock pieces. Interlayered sandstone and shale underlies the colluvium and extends up to 200m below the ground surface.  Affected by numerous folding and fault movements, the rock formation was severely fractured and exhibits no consistent joint pattern. Open end piezometers have been used to monitor the ground water table.  The groundwater could rise from its low level by more than 20 m as a result of heavy rainfalls according to available data shown in Figure 6.  The sudden and significant change in groundwater table is believed to be a major cause for the earlier slope failures in this area.
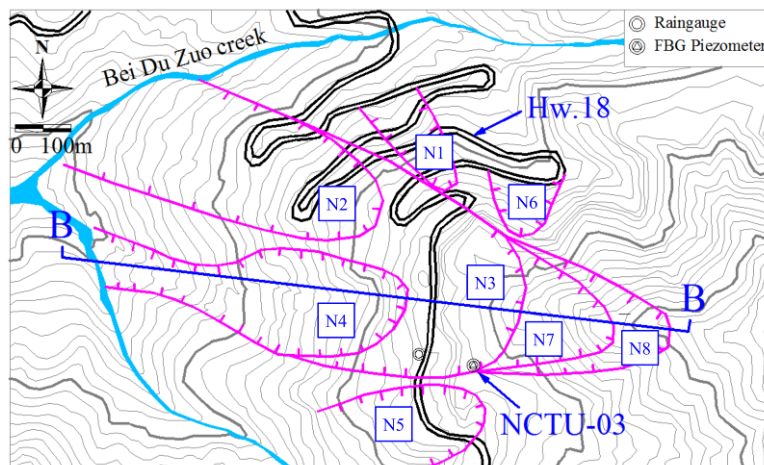


**Fig. 5 Topographic map of the Five Turn Point**
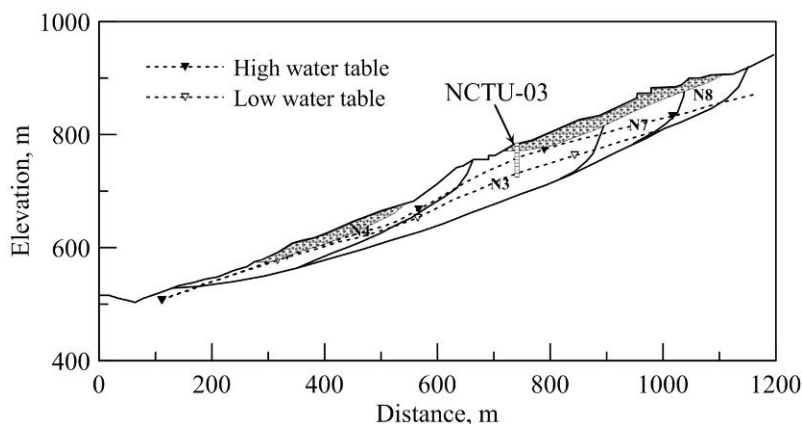**(adapted from Land Engineering Consultants, Co., Ltd., 2007).**



**Fig. 6 Section B-B of the Five Turn Point**
**(adapted from Land Engineering Consultants, Co., Ltd., 2007).**

Figure 7 shows a schematic view and photograph of an FBG pressure transducer. The FBG was used to sense the deflection of a metallic diaphragm inside of the transducer. The diaphragm separates the reference and input pressure chambers. When used as a gauge pressure transducer, the reference chamber can be sealed or exposed to the atmospheric pressure. The reference chamber is connected to a controlled reference pressure when used as a differential pressure transducer. The amount of deflection at center of the diaphragm is linearly related to the pressure difference between the reference and input pressure chambers. A separate FBG was placed inside the transducer to monitor temperature fluctuations and compensate thermal effects. The range of pressure transducer was controlled by the stiffness of the diaphragm.
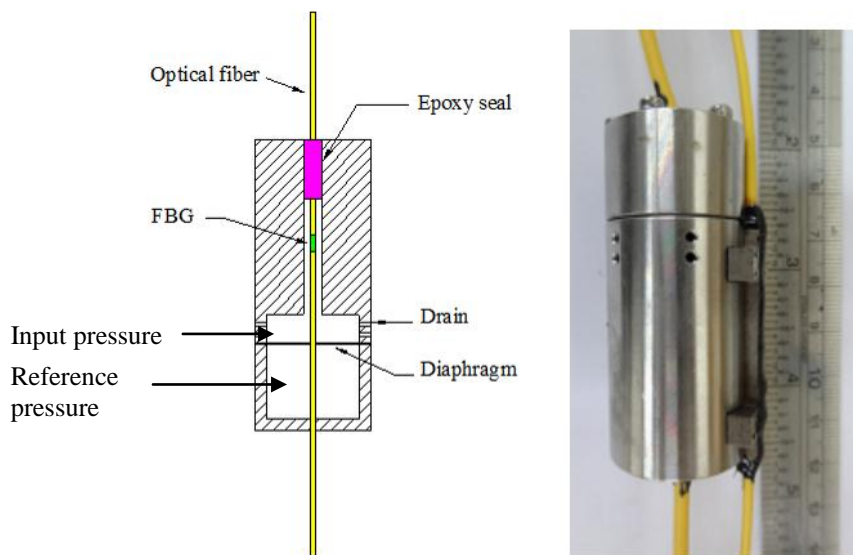


**Fig. 7 The FBG pressure transducer.**

For field measurements, the pressure transducer was converted into a piezometer by surrounding the drains with filter material. With a diameter of 25 mm, the FBG piezometer was fitted inside of a 28 mm ID and 32 mm OD PVC pipe. Small drainage holes were drilled in the PVC pipe in areas surrounding the piezometer to allow passage of water. The piezometer was epoxied and sealed at both ends in the PVC pipe to prevent seepage between piezometers from within the PVC pipe. The PVC pipe serves as a spacer and housing for the piezometers and optical fiber. All PVC pipe connectors were internal leaving a smooth exterior upon assembly in the field. A comparison between an array of FBG piezometers installed in a single borehole to the case of individual standpipes is depicted in Figure 8.

A 60m deep borehole marked as NCTU-03 in Figures 5 and 6 was used to install the FBG piezometer array. Additional PVC pipe was connected in the field to space the FBG piezometers at 5 m intervals. The segment of the PVC pipe that contained the FBG piezometer was wrapped with 1.5 m wide non-woven geotextile outside the

PVC pipe as filter.   Figure 9 shows a set of PVC pipes with FBG piezometers enclosed.   The optical fibers were threaded through the inside of the PVC pipes. The FBG piezometer array was fully assembled and inserted into the borehole with the protection of a steel casing.   The FBG piezometer was surrounded by 2 m thick sand pack (see Figure 8).   Sealing between the sand pack was provided by placing bentonite pellets.   Sand and bentonite pellets were pumped by water to the desired depth in the borehole using a 32 mm OD PVC pipe as a tremie pipe.   The deepest piezometer was located at 59 m below ground surface.   The sensors were connected to an on-site computer using optical fiber cables for optical signal interrogation and data logging/ transmission.   Field installation was completed in September, 2007.
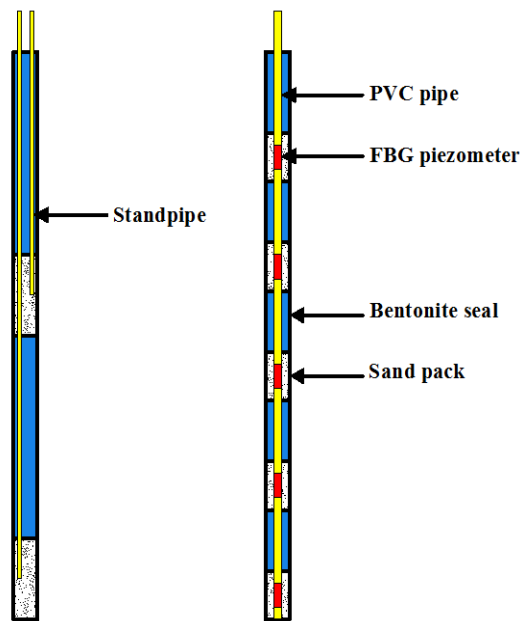


**Fig. 8 Comparison of standpipe and FBG piezometer array installations.**

The Five Turn Point slope endured three major typhoons (i.e., Sinlaku, 2008; Morakot, 2009; and Fanapi, 2010) since September 2007, and remained stable till now (May, 2012).   The following is a description of the readings taken during typhoon Morakot and their applications.

Typhoon Morakot landed in Southern Taiwan on August 8, 2009.   The histogram of daily precipitations during typhoon Morakot as shown in Figure 10 reflects an accumulated rainfall close to 3000 mm.   This is more than the average annual rainfall of 2500 mm in Taiwan.   Rainfall with intensity exceeding 700 mm/day continued through August 9, 2009.   The rain gauge with its location marked in Figure 5, was located within 100 m from the piezometer borehole (NCTU-03 of Figures 5 and 6).

**Fig. 9 PVC pipes and those with FBG piezometers enclosed.**

Figure 11 shows a set of representative pressure head ($h_p$) profiles based on the FBG piezometer readings recorded from the beginning of typhoon Morakot to the time when $h_p$ reached the maximum measurement values. The record shows that the peak pore pressure values were reached soon after the rainfall started fading on August 9. Most significant pore water pressure increase occurred in depths between 30 and 50 m. The presentation of $h_p$ profile follows the concept reported by Collins and Znidarcic (2004), except that the $h_p$ values were taken from field measurements rather than one-dimensional seepage analysis. The highly fractured rock pieces were considered as coarse granular material. Stability envelopes included in Figure 11 considered an infinitely long slope with a slope angle (β) of 23$^{°}$, indicating assumed friction angles ($\phi'$). Soil unit weight γ was assumed to be equal to twice that of water ($\gamma_w$). The $h_p$ profiles showed significant development of a perched water table at 24 m below ground surface. This phenomenon is believed to be caused by the decrease of hydraulic conductivity at the interface where the ground material changed from saturated to unsaturated state when water seeped into the ground, as described by Collins and Znidarcic (2004) for slopes with coarse material. Figure 11 demonstrates that if the ground material had a $\phi'$ less than 40$^{°}$, the slope would have failed with shear planes developed at 24 and 54 m below ground surface.

The pore water pressure readings also enabled the concept of field stress path (Anderson and Sitar, 1995; and Cascini et al., 2010) be used in evaluating the stability of the slope. The initial state of stress at each of the pore water pressure measurement locations was computed using the commercial software SIGMA/W (GEO-SLOPE, 2007). The computation was based on the cross section shown in Figure 6. The ground material was assumed to be linear elastic with Young's modulus E = 3310 MPa (estimated from an average shear wave velocity of 700 m/s according to geophysical tests), Poisson's ratio μ = 0.35, and γ = 2$\gamma_w$. For simplification, the single γ value used in the computation reflects a saturated state even when the material could be unsaturated. The potential error from the simplification of unit weight and stress-strain relationship is insignificant in

10

comparison with the stress level and the effects of pore water pressure variations (Anderson and Sitar, 1995). Considering a plane strain condition, the p (or p') and q were defined as:

$$p' = (\sigma_1' + \sigma_2' + \sigma_3')/3 \tag{5}$$

$$q = \frac{1}{\sqrt{2}} \sqrt{(\sigma_1' - \sigma_3')^2 + (\sigma_1' - \sigma_2')^2 + (\sigma_2' - \sigma_3')^2} \tag{6}$$

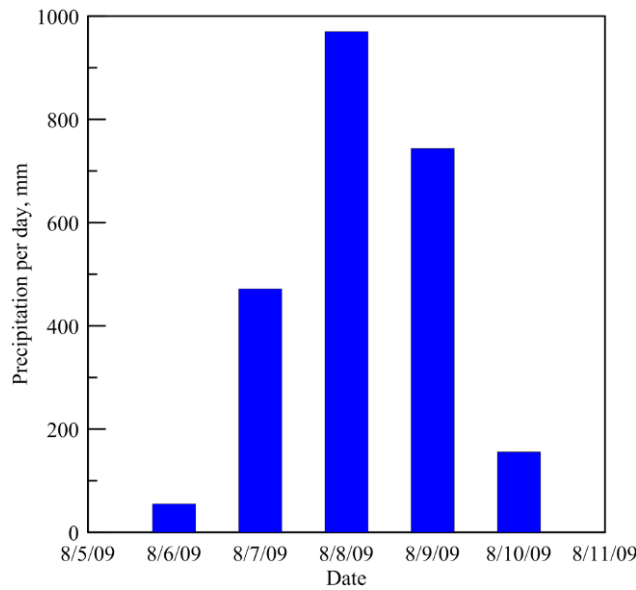where $\sigma_1'$, $\sigma_2'$, and $\sigma_3'$ = major, intermediate and minor principal stress



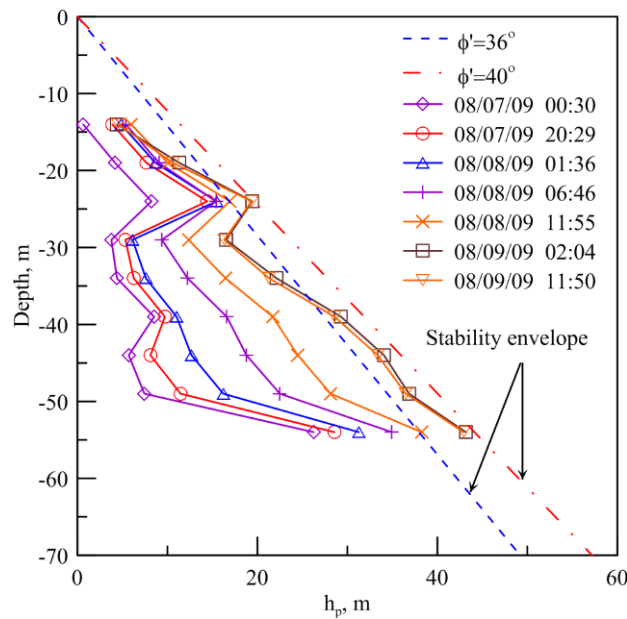**Fig. 10 Rainfall record during typhoon Morakot.**



**Fig. 11 Profile of $h_p$ during typhoon Morakot.**

As the measured pore water pressure increases, q at a given measurement point remained constant while p' decreases and the corresponding stress point (p', q) moves laterally towards a failure envelope as shown in Figure 12.   The (p', q) points depicted in Figure 12 correspond to the respective nine FBG piezometer locations installed in the field.   The lower left (p', q) points represent the state of field stress at shallower depths.   The results also show a potential failure envelope that corresponds to $\phi'$ close to $40^{\circ}$.   The advantage of field stress path approach is that it is not necessary to simplify the slope as infinitely long as in the analysis by Collins and Znidarcic (2004).   Although not necessary for the Five Turn Point case, variations in slope angle and ground layers can be readily incorporated in the analysis under the framework of field stress path.   It should be noted that the outcome of the linear elastic stress analysis was not sensitive to the selection of Young's modulus.   However, the selection of Poisson's ratio could have significant effects on the initial p, q values.

Despite the proximity to failure, there was no apparent sign of slope failure in the immediate areas surrounding borehole NCTU-03 throughout the three typhoon seasons described above.
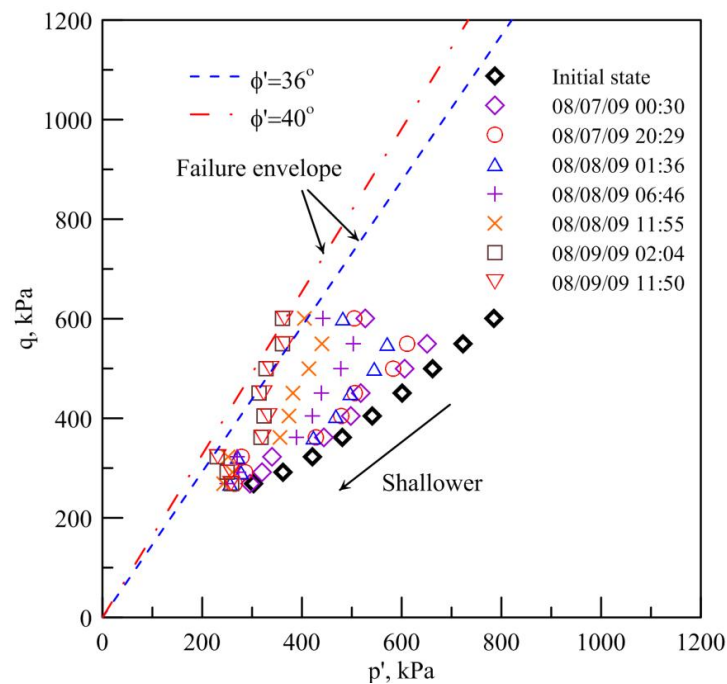


Fig. 12 Evolution of field stress paths during typhoon Morakot.

## 5.   FBG SENSORED PRESSUREMETER TESTS AT NCTU CAMPUS

The pressuremeter test (PMT) measures the relationship between its probe expansion pressure and radial strain, and hence is ideal for measuring the shear modulus − shear strain relationship (Fahey, 1998; and Wang and O'Rourke, 2007).

Currently available pre-bored PMT normally has the capability to obtain shear modulus with shear strain$\sigma$ low as $10^{-4}$, the lowest strain level other than geophysical testing methods (Mayne et al., 2002). In order to accomplish measurements with this small strain range, the PMT must be equipped with electrical radial strain and pressure sensors. The signals tend to become noisy when the strains are less than $10^{-4}$. The authors modified a pre-bored PMT originally built in our laboratory with strain gage sensored strain arms and pressure transducer. A pair of FBG attached to the spring leaf as shown in Figure 14a was used to measure expansion of the strain arms. Four strain arms separated by 90 degrees, situated at mid-level of the PMT probe were used to measure radial expansion (see Figure 14b). An FBG sensored pressure transducer similar to the one depicted in Figure 7 was used to measure PMT expansion pressure. The pressure transducer was located in a housing unit at the bottom of the PMT probe as shown in Figure 14c.



(a) Strain arms        (b) Tube section        (c) Fully asembled PMT
**Fig. 14 The FBG sensored PMT.**

Figure 15 shows the results of a PMT using the modified equipment, with two unload-reload loops following a stress controlled procedure. The test was conducted in a soft rock at the campus of National Chiao Tung University (NCTU) in Hsin Chu, Taiwan. With this system, the secant shear modulus degradation that corresponds to a minimum shear strain of $10^{-5}$ was obtained. Without digital filtering, the modulus degradation data shown in Figure 15b represent improvement in strain levels by one order of magnitude. This is mainly due to the lack of signal noises under such small strain levels and the absence of EMI. The shear wave velocities varied from 500 to 510 m/sec from suspension PS logging tests performed in the nearby borehole at comparable depths. These shear wave velocities correspond to maximum shear moduli ranging from 610 to 635 MPa.

## 6. FBG SENSORED PENETRATION TESTS IN TSENGWEN RESERVOIR

The unusually strong typhoons and heavy rainfalls that have occurred recently

caused major landslides in the watershed of Tsengwen Reservoir in Southern Taiwan, the largest hydro-project of its kind in Taiwan. Widespread landslides brought approximately 90 million m$^3$ of sediment to the Reservoir that had a storage capacity close to 600 million m$^3$ prior to typhoon Morakot of August, 2009. The debris from landslides eventually settled in the reservoir and turned into mud. From soil mechanics point of view, the mud immediately in front of the dam where the reservoir is usually the deepest is a very young, normally consolidated or under-consolidated fine grained soil. The engineering properties of the reservoir mud are important parameters in the planning and design of schemes to remove the mud. Yet, our knowledge in this regard is very limited. The depth of water above reservoir sediment at Tsengwen varies and can be close to or exceed 40m, depending on the water level. Because of the shortage of water supply, it was not possible to drain the reservoir for maintenance or soil testing purposes. Water content of the sediment may be close to or exceed its liquid limit (LL), making undisturbed soil sampling not practical. A testing program that combined field flat dilatometer tests (DMT), piezo-penetration tests and representative soil sampling was used to characterize the reservoir sediment. The aim was to establish DMT interpretation procedure for estimating soil unit weight following a framework proposed by Marchetti and Crapps (1981) that will be described later, and to use piezo-penetration to measure the excess pore water pressure and monitor the status of the mud consolidation. Figure 16 shows the plasticity and water content of soil samples retrieved from the reservoir. Representative samples from elevations above 167m, consisting of the fresh deposit brought in by typhoon Morakot were obtained using a bailer. The water content of this new sediment was as much as twice the value of its corresponding LL.
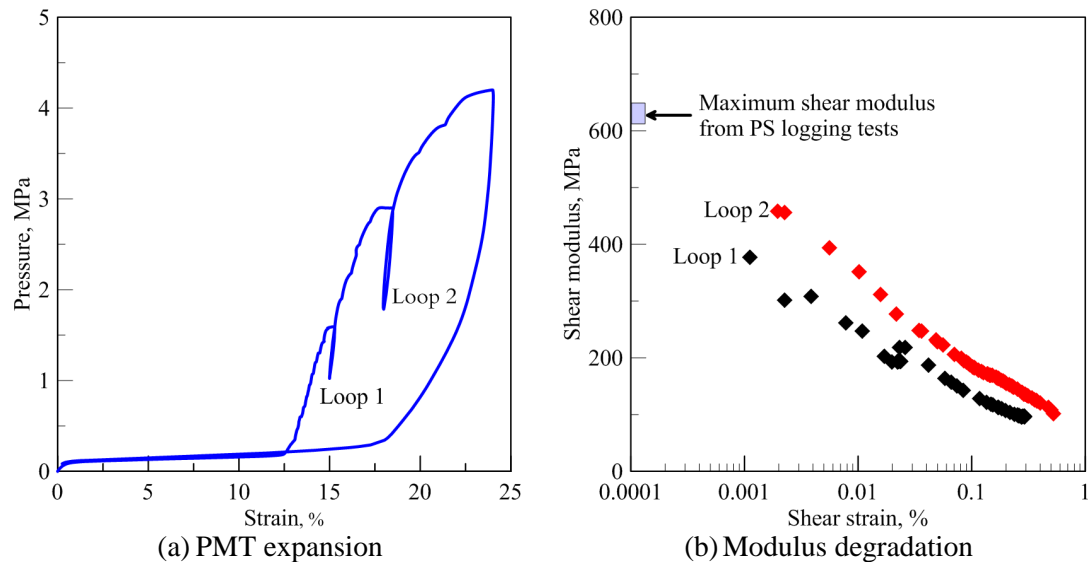


(a) PMT expansion       (b) Modulus degradation

**Fig. 15 PMT with unload-reload loops in a soft rock.**

Earlier experience by Huang and Lin (2006) has indicated that in order to facilitate DMT under deep water, it was necessary to use pneumatic electric tubing with length in excess of 70m. The relatively high in situ hydrostatic pressure ($u_o$), air

friction through the long tubing and low consistency of the soil resulted in erratic DMT lift off pressure ($p_o$) and 1.1 mm expansion pressure ($p_1$).   In extremely soft mud, the membrane stiffness values (i.e., $\Delta A$ and $\Delta B$) according to calibrations obtained from the DMT pressure control unit could result in $p_1$ less than $p_o$. Without the knowledge of excess pore water pressure in a consolidating soil deposit, the effective overburden stress, $\sigma'_{vo}$ could not be estimated with reasonable accuracy. As a result, it was not possible to obtain meaningful "intermediate" DMT parameters (Marchetti, 1980) that include material index $I_D$ (= $(p_1-p_o)/(p_o-u_o)$), horizontal stress index $K_D$ (= $(p_o-u_o)/\sigma'_{vo}$), and dilatometer modulus $E_D$ (= $34.7(p_1-p_o)$).   Because of these reasons, the authors placed a differential FBG pressure transducer immediately above the DMT blade (to be referred to as the $\Delta$DMT), as shown in Figure 17. With this set up, the DMT measurements directly reveal $(p_o-u_o)$ and $(p_1-p_o)$, irrespective of the depth of water.   $\Delta A$ and $\Delta B$ were not affected by the air friction in the pneumatic tubing as they were obtained from the FBG pressure transducer immediately above the DMT blade.   FBG signals were immune to short circuit when submerged under water.
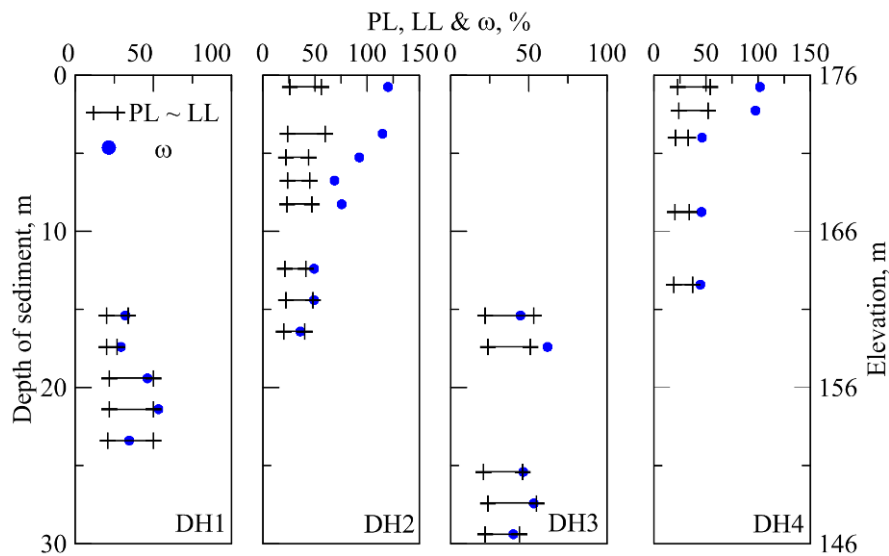


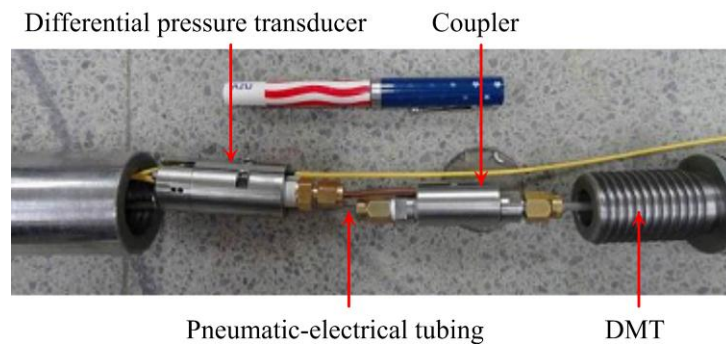**Fig. 16 Plasticity and water content of the reservoir sediment.**



**Fig. 17 The differential pressure sensing element of the $\Delta$DMT.**

Figure 18 shows the fully assembled ΔDMT just prior to insertion into water. The weight of the drill rods was enough to sink the DMT blade into the mud above elevation 167 m. Results from four profiles (DH1 and DH2, repeated twice) of ΔDMT are presented in Figure 19. The $I_D$ values correctly fall within the range of clay and silt which are consistent with the classifications performed on the representative bailer samples. Coupling $I_D$ with the unusually low $E_D$ values and the laboratory measurements of the mud unit weight (γ), the original correlations proposed by Marchetti and Crapps (1981) were extended to estimate the ratio of γ to that of water ($γ_w$) for the cases of $γ / γ_w$ = 1.4 and 1.5 of similar reservoir mud as shown in Figure 20.



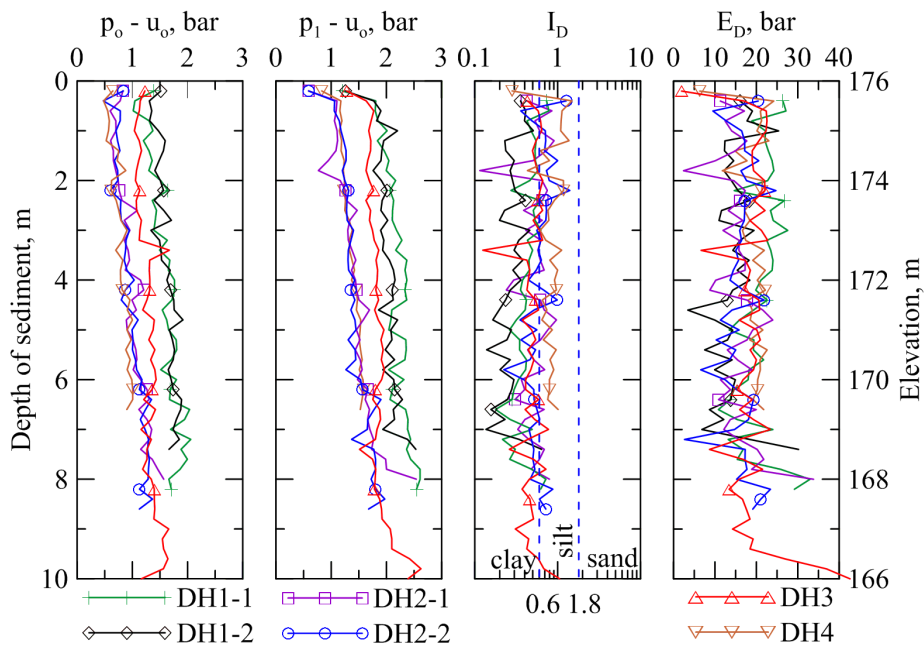**Fig. 18 The fully assembled ΔDMT.**



**Fig. 19 ΔDMT test results.**

The ΔPu (piezo-penetrometer with a differential pressure transducer) used the same FBG differential pressure transducer situated immediately above the porous element as shown in Figure 21. The penetrometer had a diameter of 35.6 mm, the same as a standard cone penetrometer. A 20 mm wide porous element was made of porous plastic with 100μm pore size. The porous element was placed at 15 mm behind the face of the $60^o$ penetrometer tip. The ΔPu measures excess pore water pressure (Δu), directly against $u_o$. Again, the readings are not affected by the depth of water. To verify the state of consolidation, ΔPu was performed in the top sediment (sediment above elevation 167 m) layer in DH4 at 50 cm intervals. The piezometer was lowered to the designated depth and the decay of excess pore water pressure was monitored. It took approximately 30 minutes for the excess pore pressure (Δu) reading to reach a stabilized value. The results of the ΔPu in terms of stabilized Δu versus depth are presented in Figure 22. The results showed that the top sediment was still in its early stage of consolidation with substantial amounts of excess pore water pressure to be dissipated and the overconsolidation ratio (OCR) for this reservoir mud was less than 1.
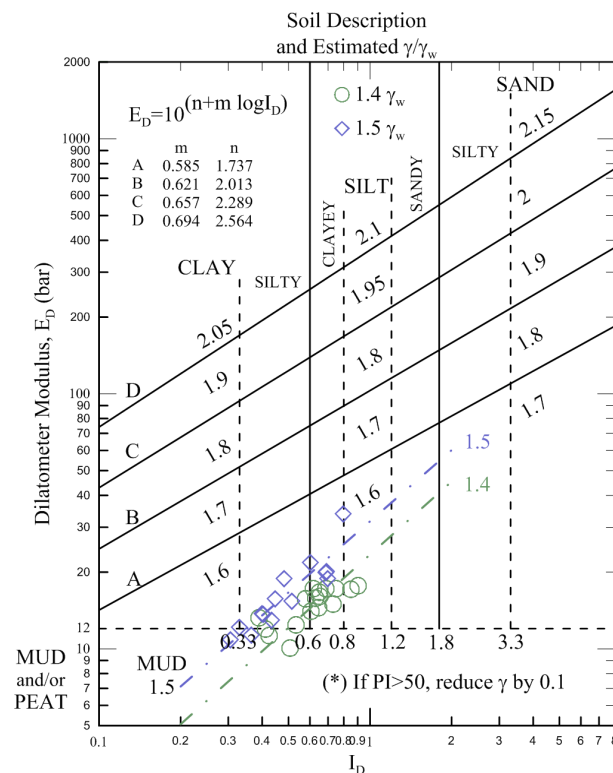


**Fig. 20 Inferring soil unit weight through $E_D$ and $I_D$ (adapted from Marchetti and Crapps, 1981).**

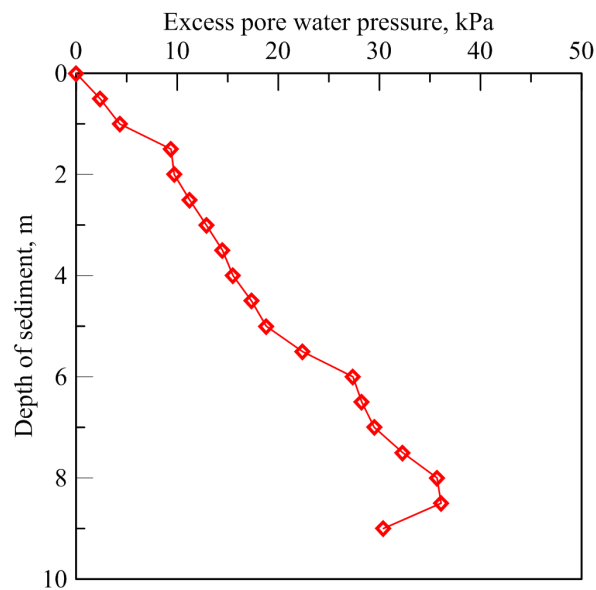**Fig. 21 The FBG sensored ΔPu.**


**Figure 22.    Excess pore water pressure from DH4.**

## 7.  FBG SENSORED TRIAXIAL TESTING DEVICE

The physical quantities involved in a triaxial testing device have mostly been monitored with electrical sensors.  Waterproofing and EMI noise filtration have often been a challenge for triaxial testing.  These drawbacks can be substantially minimized when using FBG sensors.  The authors explored the possibility of converting all pressure/force and linear displacement transducers in a conventional triaxial testing device into FBG based sensors.

The triaxial testing device was set up for tests on unsaturated soil specimens as shown in Figure 23.  The system involved three FBG gauge pressure transducers to measure the cell, pore-air and pore water pressure.  The pedestal was fitted with a high air entry ceramic to facilitate matric suction measurement.  The volume change of the unsaturated soil specimen during shearing was monitored using a double cell design (Ng et al., 2002).  Fluctuation of the water level within the inner cell caused by the specimen volume change was monitored using a FBG differential pressure transducer.  The linear displacement transducer and load cell were both mounted inside of the triaxial cell for internal measurements.  An isolated FBG was

used as a temperature sensor to monitor the fluctuation of temperature during triaxial test.

The design of the FBG displacement transducer is conceptually described in Figure 24. A bracket is bolted to the top cap. Vertical displacement of the bracket is converted into deflection of a flexible rod by pressing the bracket against a sloped surface. The amount of deflection of the flexible rod was monitored by a pair of FBG's in a scheme similar to the case of FBG-IPI. The design of FBG load cell follows the concept of a donut load cell. The force to be measured is applied at the center of a circular diaphragm with a clamped edge as shown in Figure 25. Three pairs of FBG's distributed at $120^o$ apart were attached towards the edge of the diaphragm of the load cell in the radial direction, on the opposite sides of the diaphragm to modulate the applied load and compensate temperature effects. The axial load experienced by the load cell was determined based on the average of the three pairs of the FBG's. A concentrated load applied at the center would cause the FBG's on the opposite sides of the diaphragm to experience strains in equal magnitude but opposite signs according to theory of plates and shells (Timoshenko and Woinowsky-Krieger, 1959).
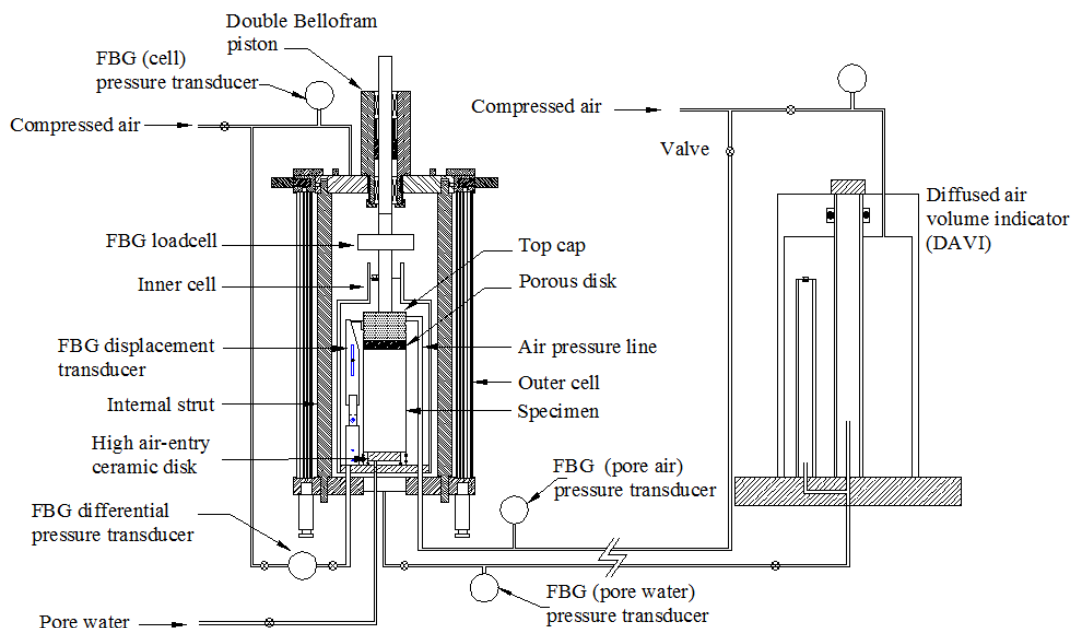


**Fig. 23 Schematic view of the triaxial testing system (adapted from Lee et al., 2011).**

An external electric load cell, electric displacement transducer (LVDT) and two electric pressure transducers (for pore water and pore air pressure measurements) were installed to provide reference readings for comparison purposes. The electric and FBG pressure transducers were connected to the same respective drainage lines. Soil samples taken from Yu Feng, a village in the watershed of Shi-Men reservoir in

Northern Taiwan was used for this series of shearing test. The non-plastic silty sand with 9% of fines (particles passing #200 sieve) had a specific gravity ($G_s$) of 2.68. The specimen prepared by wet tamping was saturated in the triaxial cell under a back pressure of 200 kPa. Upon saturation and B check, the pore-air pressure ($u_a$) was raised against the 200 kPa water back pressure to reach the desired difference between $u_a$ and pore water pressure ($u_w$), i.e., the matric suction ($u_a$-$u_w$). The cell pressure ($\sigma_c$) was raised concurrently with the $u_a$ adjustment to reach and maintain a ($\sigma_c$-$u_a$) of 100 kPa. The specimen was then allowed to drain from the bottom of the specimen and consolidate in an unsaturated state. The shearing by axial compression began when no significant drainage from the specimen could be detected. The unsaturated soil specimen was sheared using a constant water content (CW) method (Fredlund and Rahardjo, 1993). In the CW method $\sigma_c$ and $u_a$ were kept constant, while the pore water line was closed and $u_w$ was allowed to fluctuate. The axial compression was applied following a constant deformation rate of 0.01 mm per minute. The soil specimens had initial ($u_a$-$u_w$) values of 30, 90 and 200 kPa. All specimens were compacted to an initial void ratio (e) of approximately 0.5, consolidated and sheared under ($\sigma_c$-$u_a$) of 100 kPa.
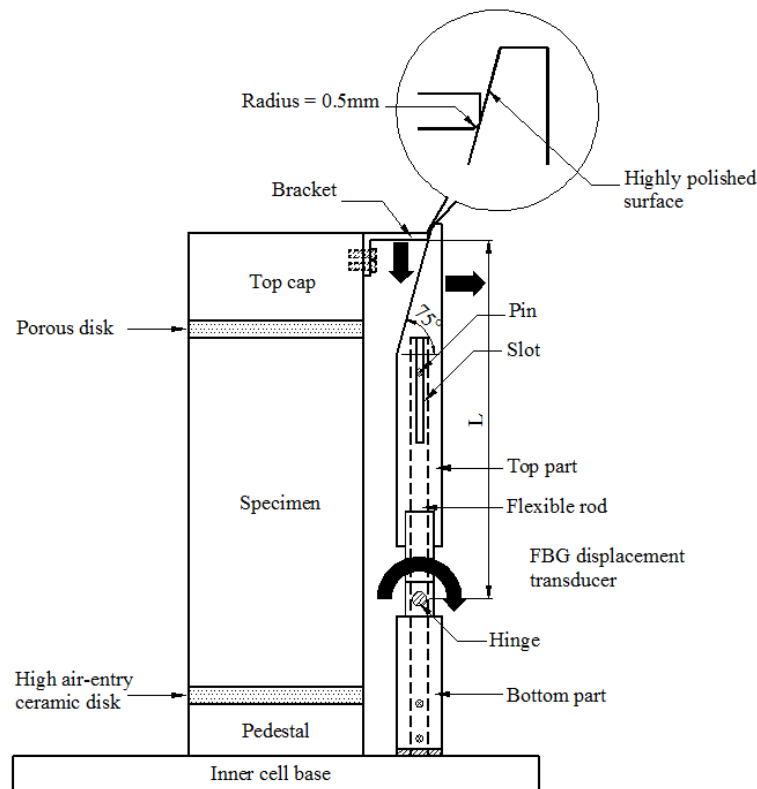


**Fig. 24 The FBG displacement transducer
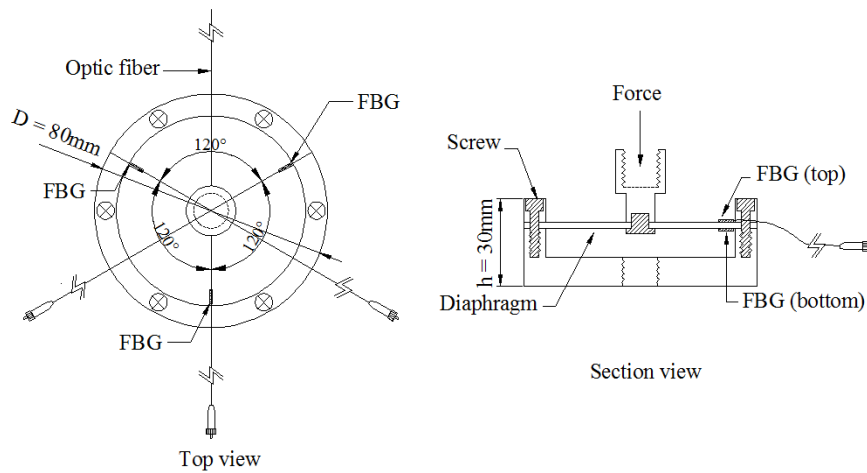(adapted from Lee et al., 2011).**

**Fig. 25 The FBG load cell (adapted from Lee et al., 2011).**

Figure 26a shows the deviator stress, excess pore water pressure and axial strain relationships from the series of triaxial tests. Results from the FBG sensors are compared with those from the corresponding electrical sensors. The matric suction change included in Figure 26b is a direct derivation of excess pore water pressure of Figure 26a. The excess pore water pressure and axial stress readings are very similar between the FBG and electrical sensors. The volumetric strain readings in Figure 26b were determined from the inner cell water fluctuation according to FBG differential pressure transducer. All specimens showed a maximum of 4 to 5% of volumetric contraction according to this series of tests. These volumetric strains correspond to a maximum of 45 mm fluctuation of water level within the inner triaxial cell. This is well within the capability of the FBG differential pressure transducer with a resolution of 0.36 mm.
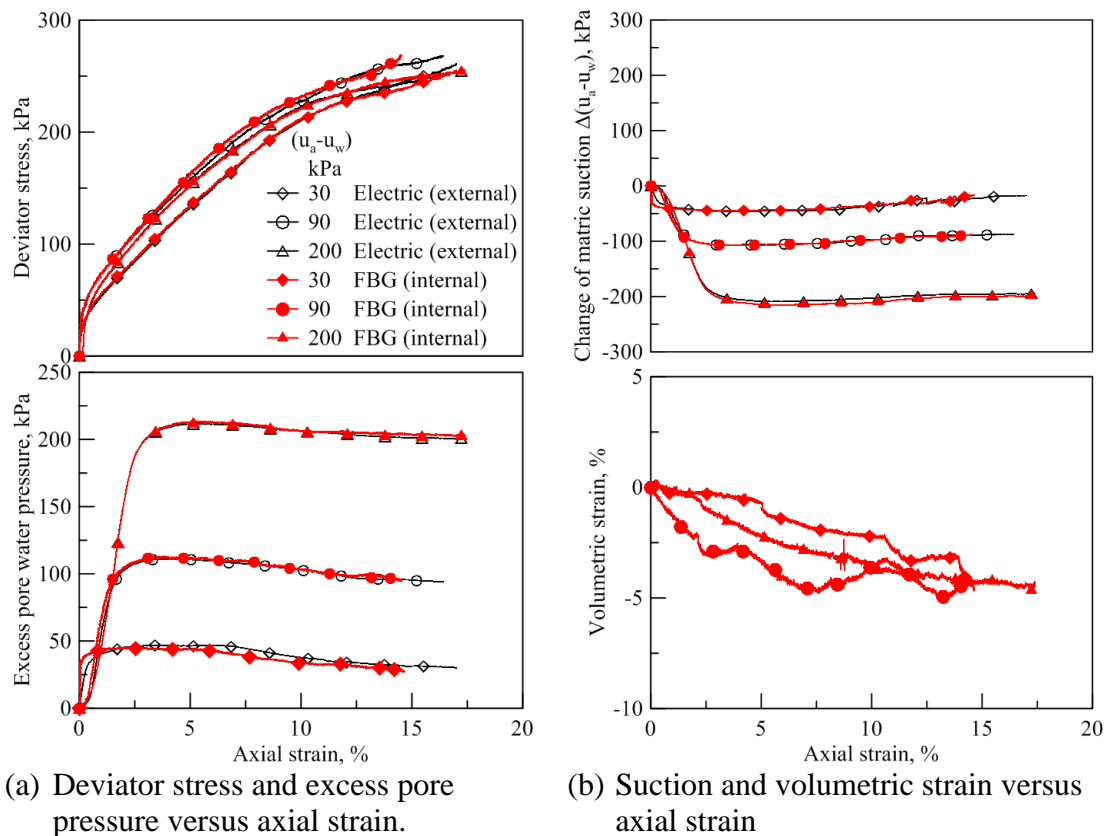
(a) Deviator stress and excess pore pressure versus axial strain.

(b) Suction and volumetric strain versus axial strain

**Fig. 26.    Triaxial test results (adapted from Lee et al., 2011).**

## 8.  CONCLUSIONS

Field hydrological and geomechanical properties/conditions are the key elements controlling the ground stability under seepage effects such as rainfall or groundwater pumping.   The FBG sensors are partially distributive, passive in nature, and they are immune to short circuit and EMI effects even when submerged under water. These unique features make FBG sensors easy to setup for automated, long term and profile monitoring in the field.   This kind of field monitoring provides a better description of the current and local soil/groundwater conditions, on a real-time basis. Results presented in the paper also demonstrated that by incorporating FBG based sensors, it is possible to extend the capabilities for some of the currently available in situ and laboratory testing devices.   Reasonable geotechnical testing results can be obtained with the help of FBG based sensors, under rather demanding conditions.

## 9.  ACKNOWLEDGEMENTS

acknowledged.

## 10. REFERENCES

Anderson, S.A., and Sitar, N. (1995). "Analysis of rainfall-induced debris flows," *Journal of Geotechnical Engineering, ASCE,* 121(7), 544-552.

Agrawal, G.P. (2002). "Fiber-optic Communication Systems, 3rd Edition" Wiley-Interscience, New York, 546p.

Cascini, L., Cuomo, S., Pastor, M., and Sorbino, G. (2010). "Modeling of Rainfall-Induced Shallow Landslides of the Flow-Type," *Journal of Geotechnical and Geoenvironmental Engineering,* 136(1), 85-98.

Collins, B.D., and Znidarcic, D. (2004). "Stability analyses of rainfall induced landslides." *Journal of Geotechnical and Geoenvironmental Engineering,* 130(4), 362-372.

Fahey, M. (1998). "Deformation and in situ stress measurement," Proc. 1st International Conference on Geotechnical Site Characterization (ISC1), Atlanta, USA, 49-68.

Fredlund, D. G., and Rahardjo, H. (1993). "Soil Mechanics for Unsaturated Soils," John Wiley & Sons, Inc., New York.

GEO-SLOPE International Ltd. (2007). "SIGMA/W for stress-deformation." Version 7.17, User's guide, Geoslope Int. Lad., Calgary, Alta., Canada.

Hill, K. O., Fujii, Y., Johnson, D. C., and Kawasaki, B. S. (1978). "Photosensitivity in Optical Fiber Waveguides: Application to Reflection Filter Fabrication," *Applied Physics Letter,* 32, 647-649.

Ho, Y.T., Huang, A.B., and Lee, J.T. (2008). "Development of a Chirped/Differential Optical Fiber Bragg Grating Pressure Sensor." *Journal of Measurement Science and Technology* (19) doi: 10.1088/0957-0233/19/4/045304.

Huang, A.B., and Lin, C.P. (2006). "TDR/DMT Characterization of a Reservoir Sediment under Water," Proc. 2nd International Conference on The Flat Dilatometer, DMT 2006, Washington, D.C., 289-294.

Kersey, A. D. (1992). "Multiplexed Fiber Optic Sensors," Proc. Fiber Optic Sensors, Boston, Massachusetts, Eric Udd, editor, sponsored by SPIE-The International Society for Optical Engineering, 200-227.

Land Engineering Consultants, Co., Ltd. (2007). "Highway 28.9K~31.5K（Five Turn Point）landslide investigation, remediation planning and safety evaluation, 3rd overall report." Department of Highway Maintenance, Section V (in Chinese).

Lee, J.T., Tien, K.C., Ho, Y.T., and Huang, A.B. (2011). "A Fiber Optic Sensored Triaxial Testing Device," *ASTM Geotechnical Testing Journal,* 34(2) DOI: 10.1520/GTJ102825.

Mayne, P.W., Christopher, B.R., and DeJong, J. (2002). "Subsurface Investigations - Geotechnical Site Characterization Reference Manual." U.S. Department of Transportation, Federal Highway Administration.

Marchetti, S. (1980). "In Situ Tests by Flat Dilatometer," *Journal of Geotechnical Engineering Division, ASCE* 106(GT3), 299-321.

Marchetti, S. and Crapps, D.K. (1981). "Flat Dilatometer Manual," Internal Report of G.P.E. Inc.

Meltz, G., Morey, W. W., and Glam, W. H. (1989). "Formation of Bragg Grating in Optical Fibers by Transverse Holographic Method," *Optical Letter,* 14, 823-825.

Ng, C. W. W., Zhan, L. T., and Cui, Y. J. (2002). "A New Simple System for Measuring Volume Changes in Unsaturated Soils," *Canadian Geotechnical Journal,* 39 757–764.

Rao, Y. -J. (1998). "Fiber Bragg Grating Sensors: Principles and Applications," Optic Fiber Sensor Technology, Edited by K.T.V. Gattan and B.T. Meggitt, Published by Chapman and Hall, London, Vol. 2, 355-379.

Timoshenko, S. P. and Woinowsky-Krieger, S. (1959). "Theory of Plates and Shells," 2nd Edition (New York: McGraw-Hill).

Wang, Y., and O'Rourke, T.D. (2007). "Interpretation of secant shear modulus degradation characteristics from pressuremeter tests," *Journal of Geotechnical and Geoenvironmental Engineering,* 133(12), 1556-1566.